

# Lattice-matched heterojunctions between topological and normal insulators: A first-principles study

Hyungjun Lee\* and Oleg V. Yazyev

*Institute of Physics, École Polytechnique Fédérale de Lausanne (EPFL), CH-1015 Lausanne, Switzerland*

(Dated: September 12, 2018)

Gapless boundary modes at the interface between topologically distinct regions are one of the most salient manifestations of topology in physics. Metallic boundary states of time-reversal-invariant topological insulators (TIs), a realization of topological order in condensed matter, have been of much interest not only due to such a fundamental nature, but also due to their practical significance. These boundary states are immune to backscattering and localization owing to their topological origin, thereby opening up the possibility to tailor them for potential uses in spintronics and quantum computing. The heterojunction between a TI and a normal insulator (NI) is a representative playground for exploring such a topologically protected metallic boundary state and expected to constitute a building block for future electronic and spintronic solid-state devices based on TIs. Here, we report a first-principles study of two experimentally realized lattice-matched heterojunctions between TIs and NIs,  $\text{Bi}_2\text{Se}_3(0001)/\text{InP}(111)$  and  $\text{Bi}_2\text{Te}_3(0001)/\text{BaF}_2(111)$ . We evaluate the band offsets at these interfaces from many-body perturbation theory within the *GW* approximation as well as density-functional theory. Furthermore, we investigate the topological interface states, demonstrating that at these lattice-matched heterointerfaces they are strictly localized and their helical spin textures are as well preserved as those at the vacuum-facing surfaces. These results taken together may help in designing devices relying on spin-helical metallic boundary states of TIs.

## I. INTRODUCTION

Interfaces have been a fertile ground for creating novel states and exploring exotic physics in the history of condensed-matter physics due to a myriad of intriguing phenomena emerging at them<sup>1–8</sup>. In addition to such a fundamental interest in interfaces, they have attracted considerable attention also from an applications standpoint. In modern solid-state devices permeating our daily life, interface formation is inevitable due to their inherent heterojunction structures, and thus thorough understanding of interface-related phenomena is indispensable for manipulating their functionality. One of the archetypal examples is the metal-oxide-semiconductor field-effect transistor (MOSFET), the workhorse of modern microelectronics<sup>9</sup>. In this regard, there have been much theoretical and experimental interest in a variety of phenomena occurring at the interface of heterojunctions such as band offsets and Schottky barriers<sup>10–12</sup>.

Rich interface physics arises also in the context of topology in condensed matter in the sense that gapless boundary states, one of the key emergent topological phenomena, manifest themselves at the interface that separates topologically distinct phases<sup>13,14</sup>. These boundary states are ensured by the different topologies of the constituent bulk phases<sup>13,14</sup>, referred to as the bulk-boundary correspondence<sup>15</sup>, and ubiquitous in various contexts of physics<sup>16,17</sup>. Initial research in condensed-matter physics along this line includes solitons in polyacetylene by Su, Schrieffer, and Heeger<sup>18</sup>, which is a condensed-matter realization of the earlier Jackiw-Rebbi model in high energy physics<sup>19</sup>, and the integer quantum Hall effect<sup>20,21</sup>. More recently, research on topology in condensed matter has been rekindled by the discovery of time-reversal-invariant topological insulators (TIs) in-

cluding the quantum spin Hall systems<sup>22–24</sup>.

Since their first theoretical proposals<sup>25–27</sup>, interest in TI has surged among both science and engineering communities owing to the fact that its topological phenomena don't require extreme conditions such as low temperatures and high external magnetic fields and not only it might serve as a route to realizing Majorana fermions and magnetic monopoles, but also its topologically protected spin-helical metallic boundary states might pave the way for future spintronics and quantum computing<sup>22,23,28</sup>. While initial research efforts had mostly been devoted to the vacuum-facing TI surfaces<sup>29–35</sup>, increasing experimental<sup>36–39</sup> and theoretical attention<sup>40–44</sup> have recently been paid to the more realistic situation, the interfaces between TIs and normal insulators (NIs). It is motivated by the fact that interfaces are protected from the possible ambient contamination<sup>45,46</sup> and moreover these types of heterojunctions can be integrated into existing semiconductor technology, hence, they are more advantageous for utilizing the topological conducting boundary states.

Among TIs realized experimentally to date, the  $\text{Bi}_2\text{Se}_3$  family compounds are prototypical on account of their simple surface-state band dispersion with the single Dirac cone and a relatively large bulk band gap of greater than 0.1 eV<sup>29–32</sup>. They are currently synthesized by using various methods such as chemical vapor deposition, Bridgman growth, and molecular beam epitaxy (MBE), and among them the MBE technique is preferable to other approaches in that it naturally allows for heterojunctions with potential solid-state-device applications<sup>47</sup>. Although it is believed that due to the van der Waals epitaxy characteristic of this class of compounds, the lattice match between TI deposit and NI substrate is not a critical factor<sup>47</sup>, small lattice mismatch is still responsible for

high-quality of TI films<sup>48–51</sup> yielding, in particular, good transport properties<sup>52</sup>.

In the present work, we consider the experimentally realized lattice-matched TI/NI heterojunctions,  $\text{Bi}_2\text{Se}_3(0001)/\text{InP}(111)$  with the lattice misfit of 0.2 %<sup>48–50</sup> and  $\text{Bi}_2\text{Te}_3(0001)/\text{BaF}_2(111)$  with that of 0.1 %<sup>51,52</sup>. For these heterojunctions, we obtain the band offsets at the interfaces via the quasiparticle  $GW$  approximation as well as semilocal density-functional theory and investigate the electronic and spin structures of topological interface states. From the calculations, we demonstrate that at these lattice-matched heterointerfaces topologically protected interface states are strictly localized and their helical spin textures are as well maintained as those at the vacuum-facing surfaces. These results taken together may help in designing future spintronic and electronic devices utilizing the topologically protected spin-helical metallic boundary states of TIs.

The remainder of this paper is organized as follows: In Sec. II, we describe computational details employed in this study. Sec. III discusses the main results of our work. Namely, in Sec. III A we introduce the interface models adopted here and in Sec. III B we describe the band offsets in heterojunctions considered and the electronic and spin structures of topological interface states. Finally, Sec. IV concludes our paper.

## II. COMPUTATIONAL METHOD

Our present study is based on *ab initio* density-functional-theory (DFT) method<sup>53,54</sup> as implemented in the QUANTUM ESPRESSO package<sup>55</sup> and many-body perturbation theory within the Hedin's  $GW$  approximation<sup>56</sup> as implemented in the YAMBO code<sup>57</sup>. In DFT calculations, the generalized gradient approximation of Perdew-Burke-Ernzerhof (PBE) type<sup>58</sup> is employed for the exchange-correlation energy and the norm-conserving pseudopotentials (PPs)<sup>59</sup> with multiple projectors per orbital angular momentum channel<sup>60</sup> are used to simulate the interaction of valence electrons with atomic cores. Spin-orbit coupling is treated by the fully-relativistic PPs<sup>61</sup> in fully separable forms<sup>62</sup>. Wave functions are expanded in terms of plane waves with the kinetic energy cutoffs of 120 Ry for  $\text{Bi}_2\text{X}_3$  ( $X=\text{Se}, \text{Te}$ ) and 180 Ry for InP,  $\text{BaF}_2$ , and all interface models. The  $\mathbf{k}$ -point meshes of  $12 \times 12 \times 1$  and  $12 \times 12 \times 12$  in the scheme of Monkhorst-Pack<sup>63</sup> are used for the Brillouin-zone sampling in interface and bulk calculations, respectively. These computational parameters were carefully checked and chosen to allow for a numerical precision of better than 0.1 meV for the total energy per atom in each case.

For the purpose of investigating the band alignment in the heterojunction between bulk materials  $A$  and  $B$

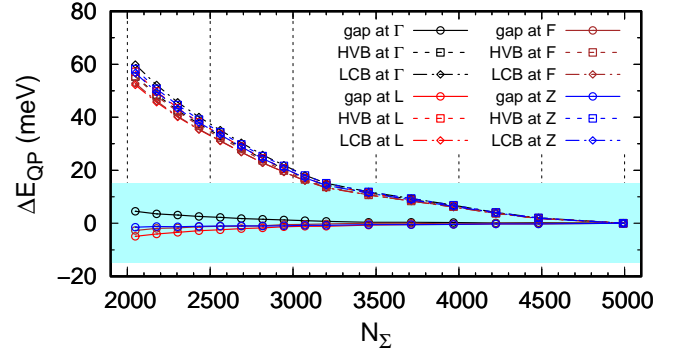


FIG. 1. (Color online) Convergence study of quasiparticle (QP) energies  $E_{\text{QP}}$  at high-symmetry  $\mathbf{k}$  points of  $2 \times 2 \times 2$  grid with respect to the number of bands  $N_{\Sigma}$  in the summation of the correlation part of the self-energy for bulk  $\text{Bi}_2\text{Se}_3$ . Here, assuming that the kinetic energy cutoff of 60 Ry for the polarizability and the number of bands of 4992 for the correlation self-energy summation are enough to reach the (numerically) converged QP energies, we plot the differences  $\Delta E_{\text{QP}}$  from them as a function of  $N_{\Sigma}$ . The HVB (LCB) represents the energy of the highest valence (lowest conduction) band; the high-symmetry  $\mathbf{k}$  points of  $\Gamma$ , L, F, and Z correspond to the  $\mathbf{k}$  points of (0,0,0), (0.5,0,0), (0.5,0.5,0), and (0.5,0.5,0.5) in reciprocal lattice units, respectively. The cyan-shaded region indicates our convergence criterion of  $\pm 15$  meV for QP energies of bulk  $\text{Bi}_2\text{Se}_3$ .

( $A/B$ ), the following expression is used<sup>64,65</sup>:

$$\begin{aligned} E_{v(c),A/B}^{\text{BO}} &= \Delta E_{\text{VBM(CBM)},A/B} + \Delta V_{A/B} \\ &= E_{\text{VBM(CBM)},A} - E_{\text{VBM(CBM)},B} + \Delta V_{A/B} \end{aligned} \quad (1)$$

for the valence (conduction)-band offset (BO), where  $E_{\text{VBM},X}$  and  $E_{\text{CBM},X}$  are, respectively, the valence-band maximum (VBM) and the conduction-band minimum (CBM) of a bulk material  $X$  ( $X = A, B$ ), and  $\Delta V_{A/B}$  is the potential lineup across the interface from  $B$  to  $A$ . The band-edge positions of  $E_{\text{VBM},X}$  and  $E_{\text{CBM},X}$  are calculated with respect to the reference of each bulk constituent  $X$  which is determined by the macroscopic average<sup>65</sup> of electrostatic potential comprising the local part of PPs and the Hartree potential through bulk calculations. The potential lineup  $\Delta V_{A/B}$  is obtained also by using the macroscopic average method through interface calculations. To be precise, in addition to DFT-PBE the band-edge position is obtained by the many-body perturbation theory within the  $GW$  approximation at the  $G_0W_0$  level<sup>66</sup>, but the potential lineup at interface is derived only from the DFT-PBE calculations, following the previous studies<sup>67,68</sup>. Finally, the band-edge positions are determined from Wannier interpolation<sup>69</sup> on a dense  $\mathbf{k}$  grid of  $100 \times 100 \times 100$  using the WANNIER90 package<sup>70</sup>.

In our  $G_0W_0$  calculations, dielectric function is calculated within the random phase approximation<sup>71,72</sup> and its frequency dependence is approximated by employing the plasmon-pole model of Godby and Needs<sup>73</sup>. In or-

TABLE I. Summary of convergence parameters for  $G_0W_0$  calculations.  $E_\chi$  stands for the kinetic energy cutoff in the plane-wave expansion of the polarizability  $\chi$  and  $N_\Sigma$  the number of both occupied and unoccupied states in the summation of the correlation part of the self-energy. In general, the number of bands required for convergence of the polarizability,  $N_\chi$ , is smaller than  $N_\Sigma$ , but for the sake of convenience we used the same value for  $N_\chi$  as  $N_\Sigma$ .

	$\mathbf{k}$ points	$E_\chi$ (Ry)	$N_\Sigma, N_\chi$
Bi <sub>2</sub> Se <sub>3</sub>	$6 \times 6 \times 6$	48	3200
Bi <sub>2</sub> Te <sub>3</sub>	$6 \times 6 \times 6$	42	3200
InP	$8 \times 8 \times 8$	50	2048
BaF <sub>2</sub>	$8 \times 8 \times 8$	48	2048

der to take fully into account the spin-orbit coupling, two-spinor wave functions from the DFT-PBE calculations are taken as inputs to the calculations of the non-interacting Green's function and the screened Coulomb interaction<sup>74</sup>. All parameters relevant to  $G_0W_0$  calculations except for the number of  $\mathbf{k}$  points were determined in calculations with the smaller  $\mathbf{k}$ -point mesh of  $2 \times 2 \times 2$  than that in actual calculations as done in the previous studies<sup>75,76</sup> and Figure 1 illustrates the convergence behavior of quasiparticle energies with respect to the number of states for the correlation self-energy summation in bulk Bi<sub>2</sub>Se<sub>3</sub>. Finally, using these obtained parameters we carried out additional convergence studies by varying the number of  $\mathbf{k}$ -point grid. Consequently, all parameters were chosen to ensure the convergence of the energies of the highest valence and lowest conduction states at the high-symmetry  $\mathbf{k}$  points to within 15 meV except for the wide-gap insulator BaF<sub>2</sub> for which the criterion

is 50 meV. They are summarized in Table I.

Before leaving this section, it is important to mention that the special construction of PPs is essential for obtaining more accurate results in  $GW$  calculations<sup>68,75,77–80</sup>. In order to describe accurately the high-energy unoccupied states, in particular necessary for  $GW$  calculations due to their slow convergence behavior with respect to the number of states<sup>81</sup>, we constructed PPs so that their scattering properties can be matched well to the all-electron counterparts up to 20 Ry above the vacuum level<sup>68,79</sup>. As an example, we show the plot of the logarithmic derivatives for Bi atom in Figure 2. Additionally, for In, Ba, and Bi atoms we constructed PPs with the whole atomic shell including semicore orbitals taken as valence so as to correctly describe the exchange contribution to the self-energy, as suggested by the previous literature<sup>75,77,78,80</sup>.

### III. RESULTS AND DISCUSSION

#### A. Interface models

We commence with the description of interface models adopted in this study for two TI/NI heterojunctions. First, for the Bi<sub>2</sub>Se<sub>3</sub>(0001)/InP(111) heterojunction we consider two heterointerface models according to the top-most atomic layer of InP(111) substrate, Bi<sub>2</sub>Se<sub>3</sub>(0001) on In-terminated InP(111) surface [hereafter InP(111)A] and on P-terminated one [hereafter InP(111)B]. Experiments indeed reveal that high-quality quintuple layers (QLs) of Bi<sub>2</sub>Se<sub>3</sub> are epitaxially grown on both InP(111)A and B surfaces by MBE<sup>49,50</sup>, whereas the previous theoretical study reported that the formation energy of Bi<sub>2</sub>Se<sub>3</sub> on InP(111)A is lower by about 0.5 eV per  $(1 \times 1)$  cell than that on InP(111)B<sup>49</sup>. For each heterointerface model, we consider a total of six different configurations consisting of combinations of the relative lateral position of atoms (three possibilities) in the interfacial atomic layers and the relative orientation (two possibilities) between NI substrate and TI deposit. Denoting the three in-plane lattice sites allowed by symmetry as A, B, and C, the former can be expressed as  $\cdots CBA/ACCBB \cdots$ ,  $\cdots ACB/ACCBB \cdots$ , and  $\cdots BAC/ACCBB \cdots$ , and the latter as  $\cdots CBA/ACCBB \cdots$  and  $\cdots BCA/ACCBB \cdots$ . Due to the noncentrosymmetric bulk structure of InP, it is not possible to construct the symmetric supercell for both of these two interface models; instead, we construct the asymmetric one in which two interfaces in supercell resulting from the periodic boundary condition are modeled with the most and second-most energetically favorable configurations determined as described later.

Second, regarding the Bi<sub>2</sub>Te<sub>3</sub>(0001)/BaF<sub>2</sub>(111) heterojunction, we consider one interface model of Bi<sub>2</sub>Te<sub>3</sub>(0001) on F-terminated BaF<sub>2</sub>(111) surface and for this model, we examine six configurations as in the case of the Bi<sub>2</sub>Se<sub>3</sub>(0001)/InP(111) heterojunction. The centrosymmetry of bulk BaF<sub>2</sub> enables us to construct the

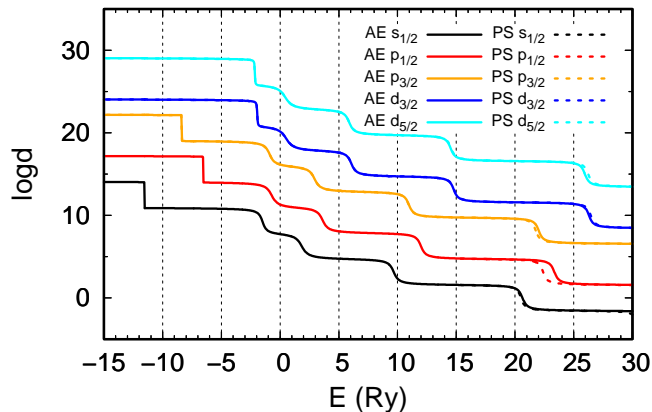


FIG. 2. (Color online) Scattering properties of Bi atom. To describe scattering properties, the logarithmic derivative ( $\log d$ ) at  $r = 3.0$  Bohr is calculated as a function of energy  $E$  using the expression of  $\arctan[r(d\psi_{l,j}/dr)/\psi_{l,j}]/\pi$ , where  $\psi_{l,j}$  is an atomic radial wave function for the state with the orbital angular momentum  $l$  and the total angular momentum  $j$ . AE and PS denote the all-electron and pseudo Bi atoms, respectively. All curves are offset for clarity.



symmetric supercell in this case.

For each interface model above, we obtain the corresponding supercell structure without vacuum by determining the lowest-energy configuration and its optimized distance between TI deposit and NI substrate. To this end, we consider the simplified interface model: the structure composed of the 13-layer InP(111) and 1-QL  $\text{Bi}_2\text{Se}_3$  slabs with the vacuum of 20 Å for the  $\text{Bi}_2\text{Se}_3(0001)/\text{InP}(111)$  heterojunction and one composed of the 18-layer  $\text{BaF}_2(111)$  and 1-QL  $\text{Bi}_2\text{Te}_3$  slabs with the vacuum of the same thickness for the  $\text{Bi}_2\text{Te}_3(0001)/\text{BaF}_2(111)$  heterojunction. Starting from these minimal models with the in-plane lattice constants of TIs (4.140 Å<sup>82</sup> and 4.386 Å<sup>83</sup> for  $\text{Bi}_2\text{Se}_3$  and  $\text{Bi}_2\text{Te}_3$ , respectively) set equal to those of NI substrates (4.134 Å<sup>84</sup> and 4.382 Å<sup>85</sup> for InP and  $\text{BaF}_2$ , respectively), we obtained the optimized distance for each configuration by calculating the total energy as a function of the distance between the blocks of  $\text{Bi}_2\text{Se}_3$  ( $\text{Bi}_2\text{Te}_3$ ) and InP ( $\text{BaF}_2$ ) and then fitting the obtained curve to the equation of state<sup>86</sup>. Finally, we determined the lowest-energy configuration for each model from comparisons among six possible configurations.

From these results, it is shown that in all simplified models, the stacking sequence rotated by 60° across the interface, i.e.,  $\cdots\text{BCA}/\text{ACCBB}\cdots$ , gives rise to the configuration with the lowest energy. As for the relative lateral position and the optimized distance, we found that the configuration with Se atoms on top of In atoms in the interfacial layers is energetically most favorable for  $\text{Bi}_2\text{Se}_3(0001)/\text{InP}(111)\text{A}$  with the distance of 2.712 Å and one with Se atoms on top of P atoms in the interfacial layers is the lowest-energy configuration for  $\text{Bi}_2\text{Se}_3(0001)/\text{InP}(111)\text{B}$  with the distance of 2.594 Å<sup>87</sup>.

For  $\text{Bi}_2\text{Te}_3(0001)/\text{BaF}_2(111)$ , the configuration with the same in-plane position of Te atoms in the interface layer and Ba atoms in the first subinterface layer is found to have the lowest energy with the distance of 3.452 Å. Using the obtained near-interface structures, in order to avoid the spurious interaction between two opposite-side interfaces, we constructed the supercell comprising 6-QL  $\text{Bi}_2\text{Se}_3$  and 37-layer InP(111)A or B, which amounts to about 120 Å in length, for  $\text{Bi}_2\text{Se}_3(0001)/\text{InP}(111)\text{A}$  or B and one comprising 6-QL  $\text{Bi}_2\text{Te}_3$  and 51-layer  $\text{BaF}_2(111)$ , amounting to about 125 Å, for  $\text{Bi}_2\text{Te}_3(0001)/\text{BaF}_2(111)$ .

## B. Electronic structures of interfaces

### 1. Band alignment

Next, we turn our attention to the electronic structures of interface models determined in Sec. III A and first study band alignment at their heterointerfaces. Figures 3(a) and 3(b) display the planar and macroscopic averages of electrostatic potential along with the ball-and-stick models of the corresponding heterojunction structures for the  $\text{Bi}_2\text{Se}_3(0001)/\text{InP}(111)\text{A}$  and B interfaces,

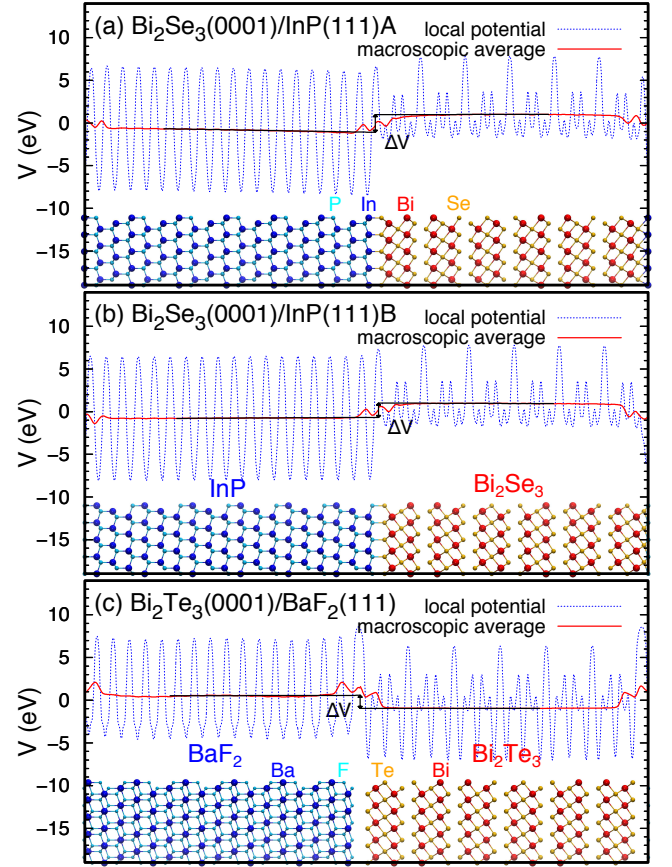


FIG. 3. (Color online) Planar and macroscopic averages of electrostatic potential for (a)  $\text{Bi}_2\text{Se}_3(0001)/\text{InP}(111)\text{A}$ , (b)  $\text{Bi}_2\text{Se}_3(0001)/\text{InP}(111)\text{B}$ , and (c)  $\text{Bi}_2\text{Te}_3(0001)/\text{BaF}_2(111)$  heterojunctions. Blue dashed lines correspond to the in-plane averaged potential along the growth direction and red solid lines the corresponding macroscopic-averaged potential. Black solid lines denote the macroscopic-averaged potential in the bulk-like region of each interface component and the resulting potential offset  $\Delta V$  at the interface is indicated by using the double-headed arrows and labels. Ball-and-stick models of heterojunction structures are given in the lower part of each panel with the atoms indicated with the corresponding labels and colors.

respectively. To obtain these potential plots, we performed the separate bulk and interface calculations as described in Sec. II. Through bulk calculations for individual bulk components of heterojunctions, we determined the reference level by use of the macroscopic average method and the band-edge positions of the VBM and CBM with respect to this reference level. Then, alignment of the each reference line in bulk components was done through interface calculations, yielding the potential lineup. In bulk calculations, we used the same structures as those used in building interface components; that is, for bulk TIs, instead of their experimental structures we used the structures whose in-plane lattice constants are set equal to those of the NI substrates. We also used the experimental structures of bulk TIs<sup>82,83</sup>, but

TABLE II. Summary of values related to the band alignment for heterojunctions considered.  $E_g^X$  represents the fundamental band gap for the bulk material X, VBO (CBO) the valence (conduction)-band offset at the interface, and  $\Delta V$  the change of macroscopic-averaged electrostatic potential across the interface. Here, VBO (CBO) and  $\Delta V$  are defined to have both positive and negative values; positive values of them indicate that the highest valence (lowest conduction) band or the macroscopic average of potential is shifted upward, crossing the interface from the NI region to the TI region. Negative values signify the opposite.

eV units	Bi <sub>2</sub> Se <sub>3</sub> (0001)/InP(111)A					Bi <sub>2</sub> Se <sub>3</sub> (0001)/InP(111)B					Bi <sub>2</sub> Te <sub>3</sub> (0001)/BaF <sub>2</sub> (111)				
	$\Delta V$	$E_g^{\text{InP}}$	$E_g^{\text{Bi}_2\text{Se}_3}$	VBO	CBO	$\Delta V$	$E_g^{\text{InP}}$	$E_g^{\text{Bi}_2\text{Se}_3}$	VBO	CBO	$\Delta V$	$E_g^{\text{BaF}_2}$	$E_g^{\text{Bi}_2\text{Te}_3}$	VBO	CBO
PBE+SO	2.08	0.72	0.29	0.65	0.22	1.68	0.72	0.29	0.25	-0.18	-1.52	6.82	0.08	3.19	-3.55
$G_0W_0$ +SO		1.42	0.21	1.01	-0.21		1.42	0.21	0.61	-0.61		9.98	0.16	5.27	-4.55

due to the small lattice mismatch, irrespective of the adopted structures, the difference in results is negligible with the order of a few meV. Because of the polar nature of InP(111)A and B blocks in our heterojunction models, the macroscopic-averaged values of potential in these systems don't tend to a constant in the bulk-like InP region far from the interface, and instead they become a linearly sloped potential in the bulk-like region, especially in the case of Bi<sub>2</sub>Se<sub>3</sub>(0001)/InP(111)A. A close look at the plot in Fig. 3(a) reveals that the macroscopic-averaged potential is linearly ramped with the slope of about 9 meV/Å. Thus, we evaluated the band offset by extending the linearly sloped macroscopic-averaged potential in the bulk-like region to the midplane between the interfacial layers and taking the value on it as proposed in the previous literature<sup>88,89</sup>.

Through interface calculations we found that electrostatic potential shifts upward by 2.08 eV and 1.68 eV, as it traverses the interface from the InP to the Bi<sub>2</sub>Se<sub>3</sub> region, for the Bi<sub>2</sub>Se<sub>3</sub>(0001)/InP(111)A and B heterojunctions, respectively. Bulk DFT-PBE calculations give the values of 0.29 eV and 0.72 eV for the band gaps of Bi<sub>2</sub>Se<sub>3</sub> and InP, respectively. These band gaps are different from the corresponding experimental values due to the well-known limitation of DFT for the prediction of band gaps and these deviations are transferred to the conduction-band offsets. As for the valence (conduction)-band offsets, from semilocal DFT-PBE calculations we obtained the values of 0.65 eV (0.22 eV) and 0.25 eV (0.18 eV) for interface A and B, respectively. Then, we corrected the band gap and band offset by using the  $G_0W_0$ -corrected band gap and band-edge positions. For instance, the  $G_0W_0$ -corrected valence (conduction)-band offset  $E_v^{G_0W_0, \text{BO}}$  ( $E_c^{G_0W_0, \text{BO}}$ ) is calculated as follows:

$$E_v^{G_0W_0, \text{BO}} = E_v^{\text{BO}} + \Delta E_{\text{VBM}}^{G_0W_0} \quad (2)$$

$$E_c^{G_0W_0, \text{BO}} = E_c^{\text{BO}} + \Delta E_{\text{CBM}}^{G_0W_0} + \Delta E_g^{G_0W_0}, \quad (3)$$

where  $E_{\text{v(c)}}^{\text{BO}}$  is the band offset at the level of DFT-PBE,  $\Delta E_{\text{VBM(CBM)}}^{G_0W_0}$  is the  $G_0W_0$ -corrected band-edge position for the valence (conduction) band, and  $\Delta E_g^{G_0W_0}$  is the  $G_0W_0$ -corrected band gap.

Performing  $G_0W_0$  calculations changes these values to, for example, 0.21 eV and 1.42 eV for a bulk band gap of Bi<sub>2</sub>Se<sub>3</sub> and InP, respectively. These calculated band

gaps are in good agreement with the experimental ones and especially, our band gaps of bulk Bi<sub>2</sub>Se<sub>3</sub> and Bi<sub>2</sub>Te<sub>3</sub> agree well with those from optical experiments<sup>90,91</sup> and those obtained from the full-potential calculation with the same treatment of spin-orbit coupling<sup>92</sup>. Putting together, we found that  $G_0W_0$  calculations change the valence (conduction)-band offset to 1.01 eV (0.21 eV) for interface A and 0.61 eV (0.61 eV) for interface B.

For the Bi<sub>2</sub>Te<sub>3</sub>(0001)/BaF<sub>2</sub>(111) heterojunction, our interface calculations have shown that electrostatic potential shifts downward by 1.52 eV, crossing the interface from the BaF<sub>2</sub> to the Bi<sub>2</sub>Te<sub>3</sub> region, and bulk DFT-PBE calculations give the band gaps of 0.08 eV and 6.82 eV for Bi<sub>2</sub>Te<sub>3</sub> and BaF<sub>2</sub>, respectively, which increase to 0.16 eV and 9.98 eV in  $G_0W_0$  calculations. For the valence (conduction)-band offset, we obtained 3.19 eV

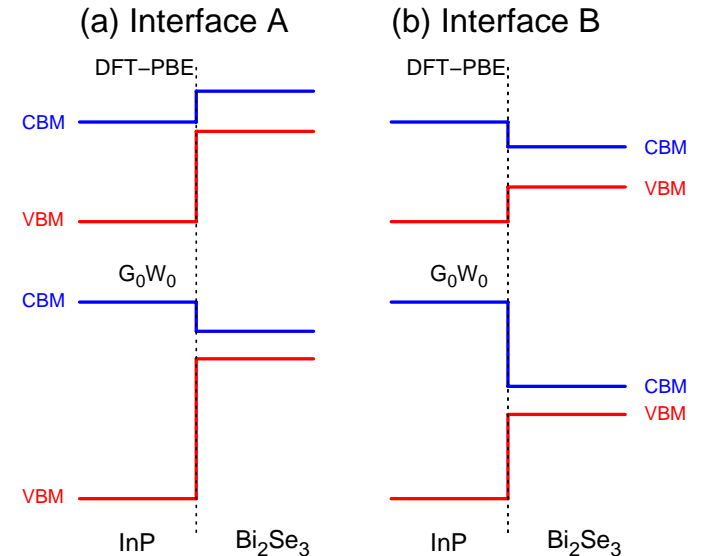


FIG. 4. (Color online) Schematic plot of the band alignment for (a) Bi<sub>2</sub>Se<sub>3</sub>(0001)/InP(111)A (Interface A) and (b) Bi<sub>2</sub>Se<sub>3</sub>(0001)/InP(111)B (Interface B). Here, the band diagrams are shown, which are obtained within both the levels of DFT-PBE and  $G_0W_0$ . The band-edge positions of VBM and CBM are indicated by the red-colored and blue-colored solid lines, respectively. Black-dashed lines correspond to the interface.

(3.55 eV) from semilocal DFT-PBE calculations which changes to 5.27 eV (4.55 eV) in  $G_0W_0$  calculations.

All results are collected in Table II and the schematic band-alignment diagrams for the two types of  $\text{Bi}_2\text{Se}_3(0001)/\text{InP}(111)$  heterojunctions are shown in Fig. 4. As can be seen from this figure, within the DFT-PBE level interface A and B show the type-II and type-I band alignment, respectively, however within the  $G_0W_0$  level, both of them exhibit the type-I band alignment.

## 2. Topological interface states

Finally, we focus on the electronic and spin structures of the topological interface states in heterojunctions considered. All results in this subsection are calculated within the DFT-PBE level. First, we identify the interface states by projecting the Kohn-Sham wave functions onto a set of localized functions defined in spheres centered at the atomic sites of the layers around the interface. The radius of sphere is set to one-half of the nearest-neighbor distance in the system and the localized function is modeled with a constant radial part multiplied by real spherical harmonics and normalized to one.

Figure 5 presents the results for two types of  $\text{Bi}_2\text{Se}_3(0001)/\text{InP}(111)$  heterojunctions. Here, the 1-QL  $\text{Bi}_2\text{Se}_3$  or the 6-layer  $\text{InP}$  closest to the interface is taken as the projection region to identify the interface states confined to within the corresponding region and the size of filled circles is proportional to the projection weight. As depicted in Figs. 5(a) and 5(b), topological interface states are clearly visible near the  $\Gamma$  point and they are mainly derived from the  $\text{Bi}_2\text{Se}_3$  side of the interface, which is in line with our expectation. In particular, the Dirac-cone character is more prominent in  $\text{Bi}_2\text{Se}_3(0001)/\text{InP}(111)\text{A}$  (Interface A) than in  $\text{Bi}_2\text{Se}_3(0001)/\text{InP}(111)\text{B}$  (Interface B), which can be attributed to the fact that in the latter  $\text{InP}$ -derived interface states are also formed near the Dirac point (DP) as seen in Fig. 5(d) and possibly hybridized with topological interface states.

Additionally, in our heterojunction models we can see the feature bearing on the vertical twinning of DPs as reported in the previous study<sup>42</sup> although the upper Dirac cone is less clear than the lower one. We also find that the location of DPs is dependent on interface details. Namely, in interface A the lower DP is located around 0.4 eV below the VBM, whereas it resides nearly at the VBM in interface B. This difference can be explained by the difference of potential lineup between interface A and B, and is consistent with the fact that interface states are subject to the band-bending effect in heterojunctions since they are usually localized within the region where potential changes abruptly (see Fig. 3)<sup>41,42</sup>.

Second, we examine the degree of localization of the topological interface states. Figure 6 shows the spatial distribution of squared wave functions of topological interface states for  $\text{Bi}_2\text{Se}_3(0001)/\text{InP}(111)\text{A}$ . As we can see

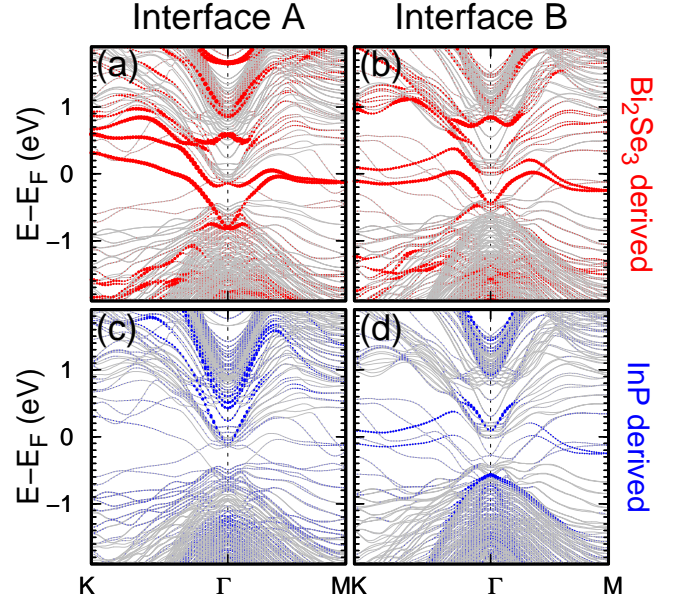


FIG. 5. (Color online) Band structures along high-symmetry  $\mathbf{k}$  directions decorated with the variable-sized dots proportional to the weights of projection of wave functions onto the near-interface region for (a,c)  $\text{Bi}_2\text{Se}_3(0001)/\text{InP}(111)\text{A}$  (Interface A) and (b,d)  $\text{Bi}_2\text{Se}_3(0001)/\text{InP}(111)\text{B}$  (Interface B). Red- and blue-colored dots represent the interface states derived from  $\text{Bi}_2\text{Se}_3$  and  $\text{InP}$  atomic layers around the interface, respectively.

in Figs. 6(a) and 6(b), the topological interface states near the DP are strictly confined to within about 12 Å around the interface and they hardly extend into the  $\text{InP}$  region. As the energy of the interface states goes away from the DP, however, they appear to start to penetrate into the  $\text{InP}$  side. For instance, the wave function of the interface state at the energy of 1.0 eV above the DP enters into the region of  $\text{InP}$ , with the third subinterface P layer having about one-tenth of its maximum density [see Figs. 6(c) and 6(d)].

Lastly, we investigate the spin structures of topological interface states. As already mentioned, the helical spin textures of topologically protected boundary states make a TI distinguishable from the integer quantum Hall system and are relevant for their application to, in particular, spintronics in which long spin coherence is crucial<sup>93</sup>. Along this line, we obtained the spin textures of topological interface states for the  $\text{Bi}_2\text{Se}_3(0001)/\text{InP}(111)\text{A}$  heterojunction by calculating the expectation values of the Pauli spin operator,  $\sigma_i$  ( $i = x, y, z$ ), for them.

Figures 7(a) and 7(b) present these results for  $\text{Bi}_2\text{Se}_3(0001)/\text{InP}(111)\text{A}$  and 6-QL  $\text{Bi}_2\text{Se}_3$ , respectively. From them, we can see that spin textures exhibit the similar tendency of a nearly circular form and a clockwise direction for the states above the DP, which is well in accord with the previous results for those at the vacuum-facing surfaces<sup>33,94</sup>. The only difference is that in the considered momentum range, the topological interface



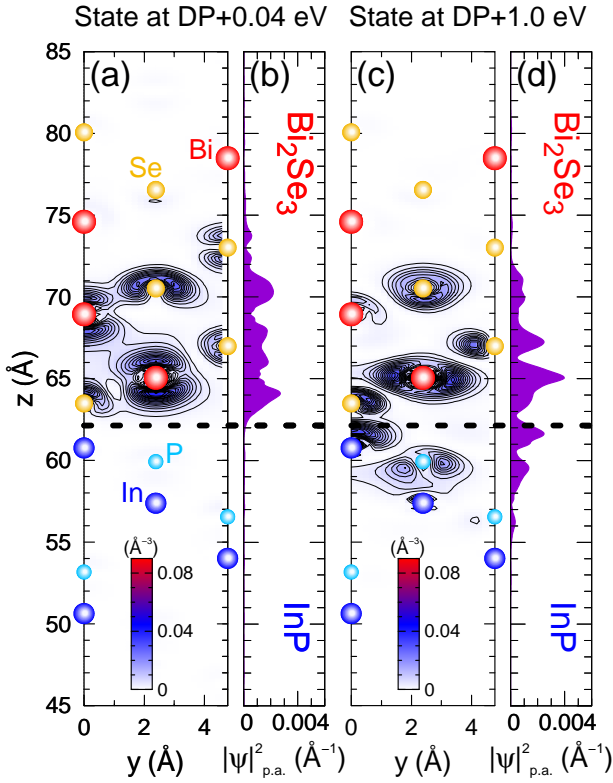


FIG. 6. (Color online) Plot of squared wave functions of the topological interface states for  $\text{Bi}_2\text{Se}_3(0001)/\text{InP}(111)\text{A}$  at the energy of (a,b) 0.04 eV and (c,d) 1.0 eV above the DP. (a) and (c) present the color-shaded contour plot in the  $x = 0$  plane, and (b) and (d) the one-dimensional planar-averaged (p.a.) plot of (a) and (c), respectively. The interval between adjacent contour lines is  $2.5 \times 10^{-3}$  per  $\text{\AA}^3$ . The atoms near the interface are marked by the balls with the corresponding colors and some of them are denoted with the labels of the same color.

states for  $\text{Bi}_2\text{Se}_3(0001)/\text{InP}(111)\text{A}$  show the less warped helical spin texture<sup>95</sup> as compared with the topological surface states at the vacuum-facing surfaces<sup>96</sup>. It can be attributed to the lowering of DP and the smaller Fermi velocity of  $3.10 \text{ eV}\cdot\text{\AA}$  than the experimentally measured value of  $3.55 \text{ eV}\cdot\text{\AA}$  of the Dirac-cone dispersion on the vacuum-facing surfaces<sup>96</sup>, which in turn induce less hybridization with the bulk states. Except for this moderate difference, our results indicate that the spin-helical structures of topological interface states are as well maintained as those at the vacuum-facing surfaces.

For the  $\text{Bi}_2\text{Te}_3(0001)/\text{BaF}_2(111)$  heterojunction, all tendencies above are similar and because of the much larger bulk band gap of  $\text{BaF}_2$ , most properties of topological interface states are indiscernible from those at the vacuum-facing surfaces.

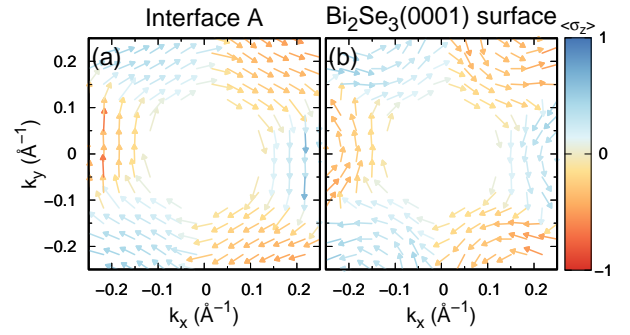


FIG. 7. (Color online) Spin textures of (a) topological interface states for  $\text{Bi}_2\text{Se}_3(0001)/\text{InP}(111)\text{A}$  (Interface A) and (b) topological surface states at the vacuum-facing surface of 6-QL  $\text{Bi}_2\text{Se}_3$  slab which is constructed from  $\text{Bi}_2\text{Se}_3(0001)/\text{InP}(111)\text{A}$  by removing the part of InP. In both cases, only states above the DP are considered. Additionally, the spin textures near the zone center are excluded since in this region the topological interface states for  $\text{Bi}_2\text{Se}_3(0001)/\text{InP}(111)\text{A}$  are buried under the bulk-like states [see Fig. 5(a)] and thus their spin textures are not well resolved. The length and direction of arrows indicate, respectively, the magnitude and direction of the expectation values of the in-plane ( $\sigma_x$  and  $\sigma_y$ ) components of the Pauli spin operator, while their color represents the normal-to-surface component ( $\sigma_z$ ).

#### IV. CONCLUSION

In summary, based on quasiparticle  $GW$  approximation as well as semilocal DFT we have presented the results of a theoretical study of the experimentally realized lattice-matched heterojunctions,  $\text{Bi}_2\text{Se}_3(0001)$  on  $\text{InP}(111)$  and  $\text{Bi}_2\text{Te}_3(0001)$  on  $\text{BaF}_2(111)$ , focusing on the band offsets at these heterointerfaces and the electronic structures and spin textures of the topological interface states. Topological interface states are shown to be strictly localized at these lattice-matched heterointerfaces. We further demonstrated that their helical spin textures are as well maintained as those at the vacuum-facing surfaces. Along with these similarities, topological interface states also exhibit some differences from topological surface states in the extent of hexagonal warping of spin textures and lowering of the DP, both of which can be ascribed to the band-bending effect occurring at the heterointerfaces of these systems. Taken collectively, our results point to the potential uses of these lattice-matched TI/NI heterojunctions in the future spintronic and electronic solid-state devices that build on topological insulators.

#### ACKNOWLEDGMENTS

We were supported by the European Research Council starting grant “TopoMat” (Grant No. 306504). First-principles computations have been performed at the

- 
- \* hyungjun.lee@epfl.ch
- <sup>1</sup> A. Ohtomo and H. Y. Hwang, *Nature* **427**, 423 (2004).
  - <sup>2</sup> S. Okamoto and A. J. Millis, *Nature* **428**, 630 (2004).
  - <sup>3</sup> N. Reyren, S. Thiel, A. D. Caviglia, L. F. Kourkoutis, G. Hammerl, C. Richter, C. W. Schneider, T. Kopp, A.-S. Retschi, D. Jaccard, M. Gabay, D. A. Muller, J.-M. Triscone, and J. Mannhart, *Science* **317**, 1196 (2007).
  - <sup>4</sup> A. D. Caviglia, S. Gariglio, N. Reyren, D. Jaccard, T. Schneider, M. Gabay, S. Thiel, G. Hammerl, J. Mannhart, and J.-M. Triscone, *Nature* **456**, 624 (2008).
  - <sup>5</sup> A. Gozar, G. Logvenov, L. F. Kourkoutis, A. T. Bollinger, L. A. Giannuzzi, D. A. Muller, and I. Bozovic, *Nature* **455**, 782 (2008).
  - <sup>6</sup> S. Valencia, A. Crassous, L. Bocher, V. Garcia, X. Moya, R. O. Cherifi, C. Deranlot, K. Bouzehouane, S. Fusil, A. Zobelli, A. Gloter, N. D. Mathur, A. Gaupp, R. Abrudan, F. Radu, A. Barthélémy, and M. Bibes, *Nat. Mater.* **10**, 753 (2011).
  - <sup>7</sup> H. Y. Hwang, Y. Iwasa, M. Kawasaki, B. Keimer, N. Nagasawa, and Y. Tokura, *Nat. Mater.* **11**, 103 (2012).
  - <sup>8</sup> J. Chakhalian, J. W. Freeland, A. J. Millis, C. Panagopoulos, and J. M. Rondinelli, *Rev. Mod. Phys.* **86**, 1189 (2014).
  - <sup>9</sup> S. M. Sze and K. K. Ng, *Physics of Semiconductor Devices*, 3rd ed. (Wiley-Interscience, Hoboken, NJ, 2006).
  - <sup>10</sup> J. Tersoff, *Phys. Rev. Lett.* **52**, 465 (1984).
  - <sup>11</sup> M. Peressi, N. Binggeli, and A. Baldereschi, *J. Phys. D: Appl. Phys.* **31**, 1273 (1998).
  - <sup>12</sup> J. Robertson, *J. Vac. Sci. Technol. A* **31**, 050821 (2013).
  - <sup>13</sup> A. Altland and B. Simons, *Condensed Matter Field Theory*, 2nd ed. (Cambridge University Press, Cambridge, England, 2010).
  - <sup>14</sup> E. Fradkin, *Field Theories of Condensed Matter Physics*, 2nd ed. (Cambridge University Press, Cambridge, England, 2013).
  - <sup>15</sup> M. Franz and L. Molenkamp, eds., *Topological Insulators*, Contemporary Concepts of Condensed Matter Science, Vol. 6 (Elsevier, Amsterdam, 2013).
  - <sup>16</sup> H. Eschrig, *Topology and Geometry for Physics*, Lecture Notes in Physics, Vol. 822 (Springer, Berlin, 2011).
  - <sup>17</sup> F. Wilczek, *Phys. Scr.* **T168**, 014003 (2016).
  - <sup>18</sup> W. P. Su, J. R. Schrieffer, and A. J. Heeger, *Phys. Rev. Lett.* **42**, 1698 (1979).
  - <sup>19</sup> R. Jackiw and C. Rebbi, *Phys. Rev. D* **13**, 3398 (1976).
  - <sup>20</sup> K. von Klitzing, G. Dorda, and M. Pepper, *Phys. Rev. Lett.* **45**, 494 (1980).
  - <sup>21</sup> D. J. Thouless, M. Kohmoto, M. P. Nightingale, and M. den Nijs, *Phys. Rev. Lett.* **49**, 405 (1982).
  - <sup>22</sup> M. Z. Hasan and C. L. Kane, *Rev. Mod. Phys.* **82**, 3045 (2010).
  - <sup>23</sup> X.-L. Qi and S.-C. Zhang, *Rev. Mod. Phys.* **83**, 1057 (2011).
  - <sup>24</sup> B. A. Bernevig and T. L. Hughes, *Topological Insulators and Topological Superconductors* (Princeton University Press, Princeton, NJ, 2013).
  - <sup>25</sup> C. L. Kane and E. J. Mele, *Phys. Rev. Lett.* **95**, 146802 (2005).
  - <sup>26</sup> C. L. Kane and E. J. Mele, *Phys. Rev. Lett.* **95**, 226801 (2005).
  - <sup>27</sup> B. A. Bernevig, T. L. Hughes, and S.-C. Zhang, *Science* **314**, 1757 (2006).
  - <sup>28</sup> J. E. Moore, *Nature* **464**, 194 (2010).
  - <sup>29</sup> D. Hsieh, D. Qian, L. Wray, Y. Xia, Y. S. Hor, R. J. Cava, and M. Z. Hasan, *Nature* **452**, 970 (2008).
  - <sup>30</sup> D. Hsieh, Y. Xia, L. Wray, D. Qian, A. Pal, J. H. Dil, J. Osterwalder, F. Meier, G. Bihlmayer, C. L. Kane, Y. S. Hor, R. J. Cava, and M. Z. Hasan, *Science* **323**, 919 (2009).
  - <sup>31</sup> D. Hsieh, Y. Xia, D. Qian, L. Wray, J. H. Dil, F. Meier, J. Osterwalder, L. Pattthey, J. G. Checkelsky, N. P. Ong, A. V. Fedorov, H. Lin, A. Bansil, D. Grauer, Y. S. Hor, R. J. Cava, and M. Z. Hasan, *Nature* **460**, 1101 (2009).
  - <sup>32</sup> Y. L. Chen, J. G. Analytis, J.-H. Chu, Z. K. Liu, S.-K. Mo, X. L. Qi, H. J. Zhang, D. H. Lu, X. Dai, Z. Fang, S. C. Zhang, I. R. Fisher, Z. Hussain, and Z.-X. Shen, *Science* **325**, 178 (2009).
  - <sup>33</sup> O. V. Yazyev, J. E. Moore, and S. G. Louie, *Phys. Rev. Lett.* **105**, 266806 (2010).
  - <sup>34</sup> K. Park, J. J. Heremans, V. W. Scarola, and D. Minic, *Phys. Rev. Lett.* **105**, 186801 (2010).
  - <sup>35</sup> C.-Y. Moon, J. Han, H. Lee, and H. J. Choi, *Phys. Rev. B* **84**, 195425 (2011).
  - <sup>36</sup> Y. Liu, H.-H. Wang, G. Bian, Z. Zhang, S. S. Lee, P. A. Fenter, J. Z. Tischler, H. Hong, and T.-C. Chiang, *Phys. Rev. Lett.* **110**, 226103 (2013).
  - <sup>37</sup> M. H. Berntsen, O. Götberg, B. M. Wojek, and O. Tjernberg, *Phys. Rev. B* **88**, 195132 (2013).
  - <sup>38</sup> R. Yoshimi, A. Tsukazaki, K. Kikutake, J. G. Checkelsky, K. S. Takahashi, M. Kawasaki, and Y. Tokura, *Nat. Mater.* **13**, 253 (2014).
  - <sup>39</sup> G. Landolt, S. Schreyeck, S. V. Eremeev, B. Slomski, S. Muff, J. Osterwalder, E. V. Chulkov, C. Gould, G. Karczewski, K. Brunner, H. Buhmann, L. W. Molenkamp, and J. H. Dil, *Phys. Rev. Lett.* **112**, 057601 (2014).
  - <sup>40</sup> G. Wu, H. Chen, Y. Sun, X. Li, P. Cui, C. Franchini, J. Wang, X.-Q. Chen, and Z. Zhang, *Sci. Rep.* **3**, 1233 (2013).
  - <sup>41</sup> V. N. Men'shov, V. V. Tugushev, S. V. Eremeev, P. M. Echenique, and E. V. Chulkov, *Phys. Rev. B* **91**, 075307 (2015).
  - <sup>42</sup> L. Seixas, D. West, A. Fazzio, and S. B. Zhang, *Nat. Commun.* **6**, 7630 (2015).
  - <sup>43</sup> Z. Chen, L. Zhao, K. Park, T. A. Garcia, M. C. Tamargo, and L. Krusin-Elbaum, *Nano Lett.* **15**, 6365 (2015).
  - <sup>44</sup> S. Küfner, L. Matthes, and F. Bechstedt, *Phys. Rev. B* **93**, 045304 (2016).
  - <sup>45</sup> D. Kong, J. J. Cha, K. Lai, H. Peng, J. G. Analytis, S. Meister, Y. Chen, H.-J. Zhang, I. R. Fisher, Z.-X. Shen, and Y. Cui, *ACS Nano* **5**, 4698 (2011).
  - <sup>46</sup> N. Kim, P. Lee, Y. Kim, J. S. Kim, Y. Kim, D. Y. Noh, S. U. Yu, J. Chung, and K. S. Kim, *ACS Nano* **8**, 1154 (2014).
  - <sup>47</sup> L. He, X. Kou, and K. L. Wang, *Phys. Status Solidi RRL* **7**, 50 (2013).
  - <sup>48</sup> N. V. Tarakina, S. Schreyeck, T. Borzenko, C. Schumacher, G. Karczewski, K. Brunner, C. Gould, H. Buhmann, and



- L. W. Molenkamp, *Cryst. Growth Des.* **12**, 1913 (2012).
- <sup>49</sup> X. Guo, Z. J. Xu, H. C. Liu, B. Zhao, X. Q. Dai, H. T. He, J. N. Wang, H. J. Liu, W. K. Ho, and M. H. Xie, *Appl. Phys. Lett.* **102**, 151604 (2013).
- <sup>50</sup> S. Schreyeck, N. V. Tarakina, G. Karczewski, C. Schumacher, T. Borzenko, C. Brne, H. Buhmann, C. Gould, K. Brunner, and L. W. Molenkamp, *Appl. Phys. Lett.* **102**, 041914 (2013).
- <sup>51</sup> O. Caha, A. Dubroka, J. Humlek, V. Hol, H. Steiner, M. Ul-Hassan, J. Snchez-Barriga, O. Rader, T. N. Stanislavchuk, A. A. Sirenko, G. Bauer, and G. Springholz, *Cryst. Growth Des.* **13**, 3365 (2013).
- <sup>52</sup> K. Hofer, C. Becker, D. Rata, J. Swanson, P. Thalmeier, and L. H. Tjeng, *Proc. Natl. Acad. Sci. U.S.A.* **111**, 14979 (2014).
- <sup>53</sup> P. Hohenberg and W. Kohn, *Phys. Rev.* **136**, B864 (1964).
- <sup>54</sup> W. Kohn and L. J. Sham, *Phys. Rev.* **140**, A1133 (1965).
- <sup>55</sup> P. Giannozzi, S. Baroni, N. Bonini, M. Calandra, R. Car, C. Cavazzoni, D. Ceresoli, G. L. Chiarotti, M. Cococcioni, I. Dabo, A. Dal Corso, S. de Gironcoli, S. Fabris, G. Fratesi, R. Gebauer, U. Gerstmann, C. Gougousis, A. Kokalj, M. Lazzeri, L. Martin-Samos, N. Marzari, F. Mauri, R. Mazzarello, S. Paolini, A. Pasquarello, L. Paulatto, C. Sbraccia, S. Scandolo, G. Sclauzero, A. P. Seitsonen, A. Smogunov, P. Umari, and R. M. Wentzcovitch, *J. Phys.: Condens. Matter* **21**, 395502 (2009).
- <sup>56</sup> L. Hedin, *Phys. Rev.* **139**, A796 (1965).
- <sup>57</sup> A. Marini, C. Hogan, M. Gruning, and D. Varsano, *Comput. Phys. Commun.* **180**, 1392 (2009).
- <sup>58</sup> J. P. Perdew, K. Burke, and M. Ernzerhof, *Phys. Rev. Lett.* **77**, 3865 (1996).
- <sup>59</sup> D. R. Hamann, M. Schlüter, and C. Chiang, *Phys. Rev. Lett.* **43**, 1494 (1979).
- <sup>60</sup> D. R. Hamann, *Phys. Rev. B* **88**, 085117 (2013).
- <sup>61</sup> L. Kleinman, *Phys. Rev. B* **21**, 2630 (1980).
- <sup>62</sup> A. Dal Corso and A. Mosca Conte, *Phys. Rev. B* **71**, 115106 (2005).
- <sup>63</sup> H. J. Monkhorst and J. D. Pack, *Phys. Rev. B* **13**, 5188 (1976).
- <sup>64</sup> C. G. Van de Walle and R. M. Martin, *Phys. Rev. B* **35**, 8154 (1987).
- <sup>65</sup> A. Baldereschi, S. Baroni, and R. Resta, *Phys. Rev. Lett.* **61**, 734 (1988).
- <sup>66</sup> M. S. Hybertsen and S. G. Louie, *Phys. Rev. B* **34**, 5390 (1986).
- <sup>67</sup> R. Shaltaf, G.-M. Rignanese, X. Gonze, F. Giustino, and A. Pasquarello, *Phys. Rev. Lett.* **100**, 186401 (2008).
- <sup>68</sup> K. Steiner, W. Chen, and A. Pasquarello, *Phys. Rev. B* **89**, 205309 (2014).
- <sup>69</sup> J. R. Yates, X. Wang, D. Vanderbilt, and I. Souza, *Phys. Rev. B* **75**, 195121 (2007).
- <sup>70</sup> A. A. Mostofi, J. R. Yates, G. Pizzi, Y.-S. Lee, I. Souza, D. Vanderbilt, and N. Marzari, *Comput. Phys. Commun.* **185**, 2309 (2014).
- <sup>71</sup> S. L. Adler, *Phys. Rev.* **126**, 413 (1962).
- <sup>72</sup> N. Wiser, *Phys. Rev.* **129**, 62 (1963).
- <sup>73</sup> R. W. Godby and R. J. Needs, *Phys. Rev. Lett.* **62**, 1169 (1989).
- <sup>74</sup> R. Sakuma, C. Friedrich, T. Miyake, S. Blügel, and F. Aryasetiawan, *Phys. Rev. B* **84**, 085144 (2011).
- <sup>75</sup> B. D. Malone and M. L. Cohen, *J. Phys.: Condens. Matter* **25**, 105503 (2013).
- <sup>76</sup> J. Klimeš, M. Kaltak, and G. Kresse, *Phys. Rev. B* **90**, 075125 (2014).
- <sup>77</sup> M. Rohlfing, P. Krüger, and J. Pollmann, *Phys. Rev. Lett.* **75**, 3489 (1995).
- <sup>78</sup> A. Marini, G. Onida, and R. Del Sole, *Phys. Rev. Lett.* **88**, 016403 (2001).
- <sup>79</sup> M. Shishkin and G. Kresse, *Phys. Rev. B* **74**, 035101 (2006).
- <sup>80</sup> P. Umari and S. Fabris, *J. Chem. Phys.* **136**, 174310 (2012).
- <sup>81</sup> B.-C. Shih, Y. Xue, P. Zhang, M. L. Cohen, and S. G. Louie, *Phys. Rev. Lett.* **105**, 146401 (2010).
- <sup>82</sup> S. Roy, H. L. Meyerheim, K. Mohseni, A. Ernst, M. M. Otrokov, M. G. Vergniory, G. Mussler, J. Kampmeier, D. Grützmacher, C. Tusche, J. Schneider, E. V. Chulkov, and J. Kirschner, *Phys. Rev. B* **90**, 155456 (2014).
- <sup>83</sup> S. Nakajima, *J. Phys. Chem. Solids* **24**, 479 (1963).
- <sup>84</sup> C. S. Menoni and I. L. Spain, *Phys. Rev. B* **35**, 7520 (1987).
- <sup>85</sup> A. S. Radtke and G. E. Brown, *Am. Mineral.* **59**, 885 (1974).
- <sup>86</sup> P. Vinet, J. H. Rose, J. Ferrante, and J. R. Smith, *J. Phys.: Condens. Matter* **1**, 1941 (1989).
- <sup>87</sup> In order to assess the influence of van der Waals correction, we carried out calculations using the semiempirical method by Grimme (PBE-D2) [S. Grimme, *J. Comput. Chem.* **27**, 1787 (2006)]. While PBE-D2 leads to the certain decrease of the interatomic distances at the interface of our heterojunction models, we found that our main results obtained with DFT-PBE still hold.
- <sup>88</sup> S. Picozzi, A. Continenza, and A. J. Freeman, *Phys. Rev. B* **55**, 13080 (1997).
- <sup>89</sup> N. R. D'Amico, G. Cantele, C. A. Perroni, and D. Ninno, *J. Phys.: Condens. Matter* **27**, 015006 (2015).
- <sup>90</sup> M. Orlita, B. A. Piot, G. Martinez, N. K. S. Kumar, C. Faugeras, M. Potemski, C. Michel, E. M. Hankiewicz, T. Brauner, Č. Drašar, S. Schreyeck, S. Grauer, K. Brunner, C. Gould, C. Brüne, and L. W. Molenkamp, *Phys. Rev. Lett.* **114**, 186401 (2015).
- <sup>91</sup> G. A. Thomas, D. H. Rapkine, R. B. Van Dover, L. F. Mattheiss, W. A. Sunder, L. F. Schneemeyer, and J. V. Waszczak, *Phys. Rev. B* **46**, 1553 (1992).
- <sup>92</sup> I. Aguilera, C. Friedrich, and S. Blügel, *Phys. Rev. B* **88**, 165136 (2013).
- <sup>93</sup> S. A. Wolf, D. D. Awschalom, R. A. Buhrman, J. M. Daughton, S. von Molnár, M. L. Roukes, A. Y. Chtchelkanova, and D. M. Treger, *Science* **294**, 1488 (2001).
- <sup>94</sup> S. R. Park, J. Han, C. Kim, Y. Y. Koh, C. Kim, H. Lee, H. J. Choi, J. H. Han, K. D. Lee, N. J. Hur, M. Arita, K. Shimada, H. Namatame, and M. Taniguchi, *Phys. Rev. Lett.* **108**, 046805 (2012).
- <sup>95</sup> L. Fu, *Phys. Rev. Lett.* **103**, 266801 (2009).
- <sup>96</sup> K. Kuroda, M. Arita, K. Miyamoto, M. Ye, J. Jiang, A. Kimura, E. E. Krasovskii, E. V. Chulkov, H. Iwasawa, T. Okuda, K. Shimada, Y. Ueda, H. Namatame, and M. Taniguchi, *Phys. Rev. Lett.* **105**, 076802 (2010).